lation between brightness and vertical flow direction (*12*). This constitutes evidence for a convective flow pattern that transports the energy flux emitted in the penumbra. Other studies show a correlation between intensity and line-of-sight velocities (*13*), which for sunspots observed outside the center of the solar disk is dominated by the horizontal Evershed flow. This is consistent with our findings, because in the penumbra the horizontal flow velocity is correlated with the vertical flow direction.

Our detailed analysis (*8*) shows that the spatial scales of the flows providing the major part of the convective energy transport are similar for both undisturbed granulation and penumbra. The primary difference is that there is no preferred horizontal direction for granulation, whereas the energy-transporting flows in the penumbra are distinctly asymmetric: Convective structures are elongated in the radial direction of the sunspot. These properties were already indicated in earlier simulations (*5*, *6*) and suggested as an explanation for the Evershed outflow in (*14*). The simulation shown here confirms this suggestion and demonstrates the convective nature of a fully developed penumbra.

The horizontal asymmetry of the convective flows is also manifest in the correlation of 0.42 between the corresponding flow component (v_x) and the brightness. We find that the rms of the outflowing velocity component (v_x) in the penumbra is much larger than the transverse component (v_y) (perpendicular to the filament direction), showing an asymmetry similar to that found by the scale analysis. The total rms velocity profile as a function of depth is very similar to its counterpart for undisturbed granulation, apart from a slightly higher peak value, confirming the physical similarity of convection in granulation and penumbra.

The mass flux and energy flux show similar properties with respect to the length scales and asymmetry (*8*), indicating that most of the outflowing material emerges, turns over, and descends within the penumbra. In the deeper layers, there is some contribution (of the order of 10 to 20%) to both energy and mass fluxes by the large-scale flow cell surrounding the sunspots.

The analysis of our simulations indicates that granulation and penumbral flows are similar with regard to energy transport; the asymmetry between the horizontal directions and the reduced overall energy flux reflect the constraints imposed on the convective motions by the presence of a strong and inclined magnetic field. The development of systematic outflows is a direct consequence of the anisotropy, and the similarities between granulation and penumbral flows strongly suggest that driving the Evershed flow does not require physical processes that go beyond the combination of convection and anisotropy introduced by the magnetic field. Weaker laterally overturning flows perpendicular to the main filament direction explain the apparent twisting motions observed in some filaments (*15*, *16*) and lead to a weakening of the magnetic field in the flow channels through flux expulsion (*6*).

Although our simulation of large sunspots is realistic in terms of relevant physics, it does not faithfully reproduce all aspects of the morphology of observed penumbral filaments. The penumbral regions are considerably more extended than in previous local simulations, but they are still somewhat subdued, probably owing to the proximity of the periodic boundaries. The filaments in the inner penumbrae appear to be too fragmented, and short, dark lanes along bright filaments (*17*) form only occasionally, likely a consequence of the still-limited spatial resolution of the simulation. Lastly, the initial condition of the magnetic field underlying the sunspot is quite arbitrary, owing to our ignorance of the subsurface structure of sunspots. Notwithstanding these limitations, the present simulations are consistent with observations of global sunspot properties, penumbral structure, and systematic radial outflows. These and earlier simulations (*5*, *6*, *10*) suggest a unified physical explanation for umbral dots as well as inner and outer penumbrae in terms of magnetoconvection in a magnetic field with varying inclination. Furthermore, a consistent physical picture of all observational characteristics of sunspots and their surroundings is now emerging.

References and Notes

1. S. K. Solanki, *Astron. Astrophys. Rev.* **11**, 153 (2003).
2. J. H. Thomas, N. O. Weiss, *Annu. Rev. Astron. Astrophys.* **42**, 517 (2004).
3. J. Evershed, *Mon. Not. R. Astron. Soc.* **69**, 454 (1909).
4. J. H. Thomas, N. O. Weiss, *Sunspots and Starspots* (Cambridge Univ. Press, Cambridge, 2008).
5. T. Heinemann, Å. Nordlund, G. B. Scharmer, H. C. Spruit, *Astrophys. J.* **669**, 1390 (2007).
6. M. Rempel, M. Schüssler, M. Knölker, *Astrophys. J.* **691**, 640 (2009).
7. M. Kubo, T. Shimizu, S. Tsuneta, *Astrophys. J.* **659**, 812 (2007).
8. More detailed information about the physical model, the numerical code, and the simulation setup is available as supporting material on *Science* Online.
9. R. Keppens, V. Martinez Pillet, *Astron. Astrophys.* **316**, 229 (1996).
10. M. Schüssler, A. Vögler, *Astrophys. J. Lett.* **641**, L73 (2006).
11. D. Dialetis, P. Mein, C. E. Alissandrakis, *Astron. Astrophys.* **147**, 93 (1985).
12. J. Sánchez Almeida, I. Márquez, J. A. Bonet, I. Domínguez Cerdeña, *Astrophys. J.* **658**, 1357 (2007).
13. L. R. Bellot Rubio, R. Schlichenmaier, A. Tritschler, *Astron. Astrophys.* **453**, 1117 (2006).
14. G. B. Scharmer, Å. Nordlund, T. Heinemann, *Astrophys. J. Lett.* **677**, L149 (2008).
15. K. Ichimoto *et al.*, *Science* **318**, 1597 (2007).
16. V. Zakharov, J. Hirzberger, T. Riethmüller, S. Solanki, P. Kobel, *Astron. Astrophys.* **488**, L17 (2008).
17. G. B. Scharmer, B. V. Gudiksen, D. Kiselman, M. G. Löfdahl, L. H. M. Rouppe van der Voort, *Nature* **420**, 151 (2002).

18. High-performance computing resources were provided by NCAR's Computational and Information Systems Laboratory. NCAR is sponsored by NSF.

Supporting Online Material

www.sciencemag.org/cgi/content/full/1173798/DC1
Materials and Methods
SOM Text
Figs. S1 to S4
References
Movies S1 and S2

19 March 2009; accepted 8 June 2009
Published online 18 June 2009;
10.1126/science.1173798
Include this information when citing this paper.

Quantum Walk in Position Space with Single Optically Trapped Atoms

Michal Karski,* Leonid Förster, Jai-Min Choi, Andreas Steffen, Wolfgang Alt, Dieter Meschede, Artur Widera*

The quantum walk is the quantum analog of the well-known random walk, which forms the basis for models and applications in many realms of science. Its properties are markedly different from the classical counterpart and might lead to extensive applications in quantum information science. In our experiment, we implemented a quantum walk on the line with single neutral atoms by deterministically delocalizing them over the sites of a one-dimensional spin-dependent optical lattice. With the use of site-resolved fluorescence imaging, the final wave function is characterized by local quantum state tomography, and its spatial coherence is demonstrated. Our system allows the observation of the quantum-to-classical transition and paves the way for applications, such as quantum cellular automata.

Interference phenomena with microscopic particles are a direct consequence of their quantum-mechanical wave nature (*1*–*5*). The prospect to fully control quantum properties of atomic systems has stimulated ideas to engineer quantum states that would be useful for applications in quantum information processing, for example, and also would elucidate fundamental questions, such as the quantum-to-classical transition (*6*). A prominent example of state engineering by controlled multipath interference is the quantum walk of a particle (*7*). Its classical counterpart, the random walk, is relevant in many aspects of our lives, providing insight into diverse fields: It forms the basis for algorithms (*8*), describes diffusion processes in physics or biology (*8*, *9*), such as Brownian motion, or has been used as a model for stock market prices (*10*). Similarly, the quantum walk is expected to have

Institut für Angewandte Physik der Universität Bonn Wegelerstraße 8, 53115 Bonn, Germany.

*To whom correspondence should be addressed. E-mail: karski@uni-bonn.de (M.K.); widera@uni-bonn.de (A.W.)

implications for various fields, for instance, as a primitive for universal quantum computing (*11*), systematic quantum algorithm engineering (*12*), or for deepening our understanding of the efficient energy transfer in biomolecules for photosynthesis (*13*).

Quantum walks have been proposed to be observable in several physical systems (*12*, *14*, *15*). Special realizations have been reported in either the populations of nuclear magnetic resonance samples (*16*, *17*) or in optical systems, in either frequency space of a linear optical resonator (*18*), with beam splitters (*19*), or in the continuous tunneling of light fields through waveguide lattices (*20*). Recently, a three-step quantum walk in the phase space of trapped ions has been observed (*21*). However, the coherent walk of an individual quantum particle with controllable internal states, as originally proposed by Feynman (*22*), has so far not been observed. We present the experimental realization of such a single quantum particle walking in a one-dimensional (1D) lattice in position space. This basic example of a walk provides all of the relevant features necessary to understand the fundamental properties and differences of the quantum and classical regimes. For example, the atomic wave function resulting from a quantum walk exhibits delocalized coherence, which reflects the underlying quantum interference. Simultaneous detection of internal state and the atomic position in the lattice by an optical microscope allows for local quantum state tomography of the wave function. This is an important requirement to realize applications in quantum information science, such as the quantum cellular automaton (*23*–*25*).

In the classical random walk on a line, a coin is tossed in each time step. Depending on the outcome (heads or tails), a walker takes one step to the left or to the right. After N time steps, the probability of finding the walker at a certain site on the line follows a binomial distribution with a width increasing proportional to $\sqrt{N}$.

In the quantum case, the walker can be brought in a coherent superposition of going to the right or left. This can be realized by adding internal states to the walker, providing an additional degree of freedom, which can be used to control the system. We consider a two-level particle with internal states $|0\rangle$ and $|1\rangle$. In every step of the walk, the coin operator brings each internal state into a coherent superposition of the two states. The essence of the general quantum walk is to entangle this internal state with the position of the corresponding wave packet by a state-dependent transport. This can be realized by shifting both internal states into opposite directions, which coherently delocalizes the particle over two lattice sites. Repetition of the unitary coin-shift operation sequence results in the so-called

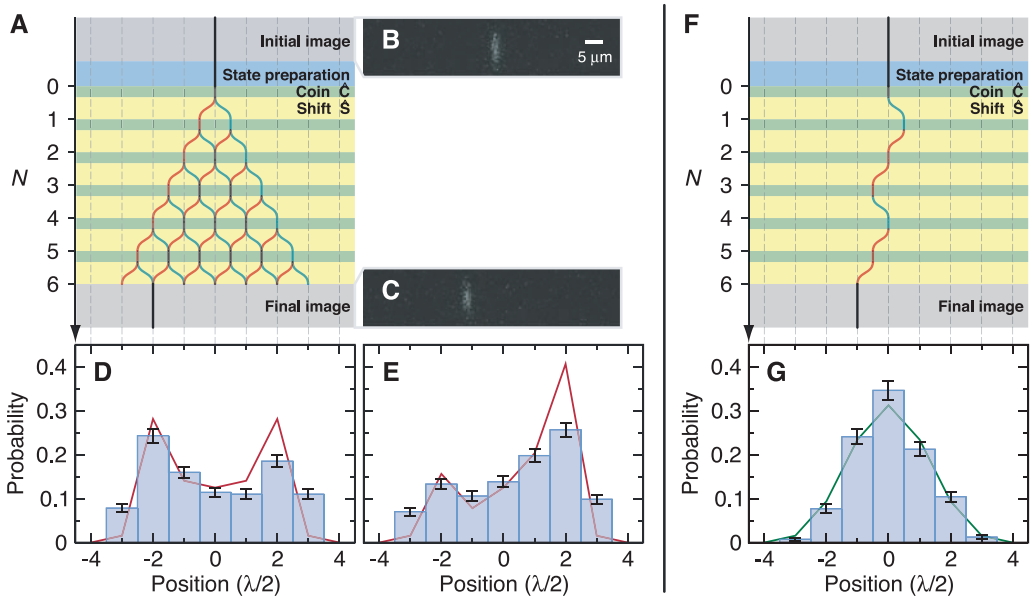

Fig. 1. (**A**) Schematic experimental sequence for the quantum walk showing the paths for the internal states $|0\rangle$ (green) and $|1\rangle$ (red). The walking distance is extracted from the initial (**B**) and final (**C**) fluorescence image. The results of several hundreds of identical realizations form the probability distribution, which is symmetric for the initial state $(|0\rangle + i|1\rangle)/\sqrt{2}$ (**D**) and antisymmetric for the initial state $|1\rangle$ (**E**). The analogous random walk sequence (**F**) yields a binomial probability distribution (**G**). The displayed path is one of many random paths that the atom can take. Measured data are shown as a histogram, and the theoretical expectation for the ideal case is denoted with a solid line. Error bars indicate the statistical $\pm 1\sigma$ uncertainty.

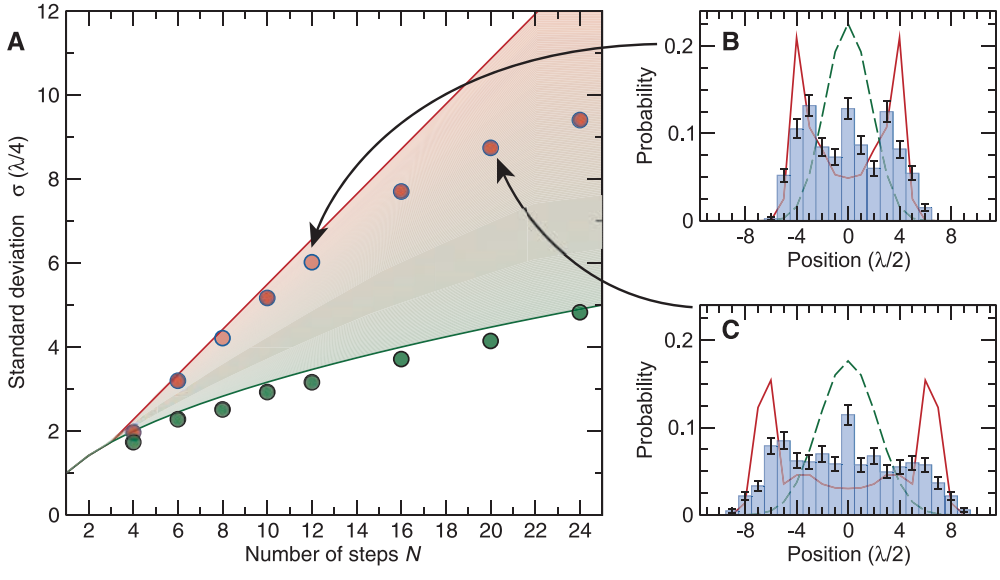

Fig. 2. (**A**) Scaling of the SD of the measured spatial probability distributions for quantum walk (red) and random walk (green). The solid lines indicate the expectations for the ideal cases. Error bars are smaller than the size of symbols. The measured quantum walks follow the ideal linear behavior until, because of decoherence, they gradually turn into a random walk. The probability distributions for N = 12 (**B**) and N = 20 (**C**) show a gradual change from the quantum to a classical shape. The theoretical prediction is shown as a solid line for the pure quantum walk and as a dashed line for the random walk.

quantum walk. After two steps of the quantum walk, two parts of the wave function are recombined at a common lattice site. Being in different internal states, they cannot interfere. The next coin operator, however, mixes the internal states in a deterministic way, which gives rise to quantum interference of the two overlapping wave packets. Further steps result in a multipath interference (Fig. 1A), which then alters the properties of the quantum walk as compared with the classical random walk. In particular, the width of the probability distribution to find the walker at a certain position scales proportional to N for the quantum walk, as in a ballistic transport, in contrast to the diffusive $\sqrt{N}$ scaling of the random walk. The influence of internal states on the quantum walk provides another distinguishing feature: Whereas the probability distribution of the random walk is fully determined by the balance of the coin, the quantum walk distribution strongly depends on the initial internal state of the walker and can be either symmetric or strongly asymmetric for one and the same coin operator (Fig. 1). Furthermore, as the quantum

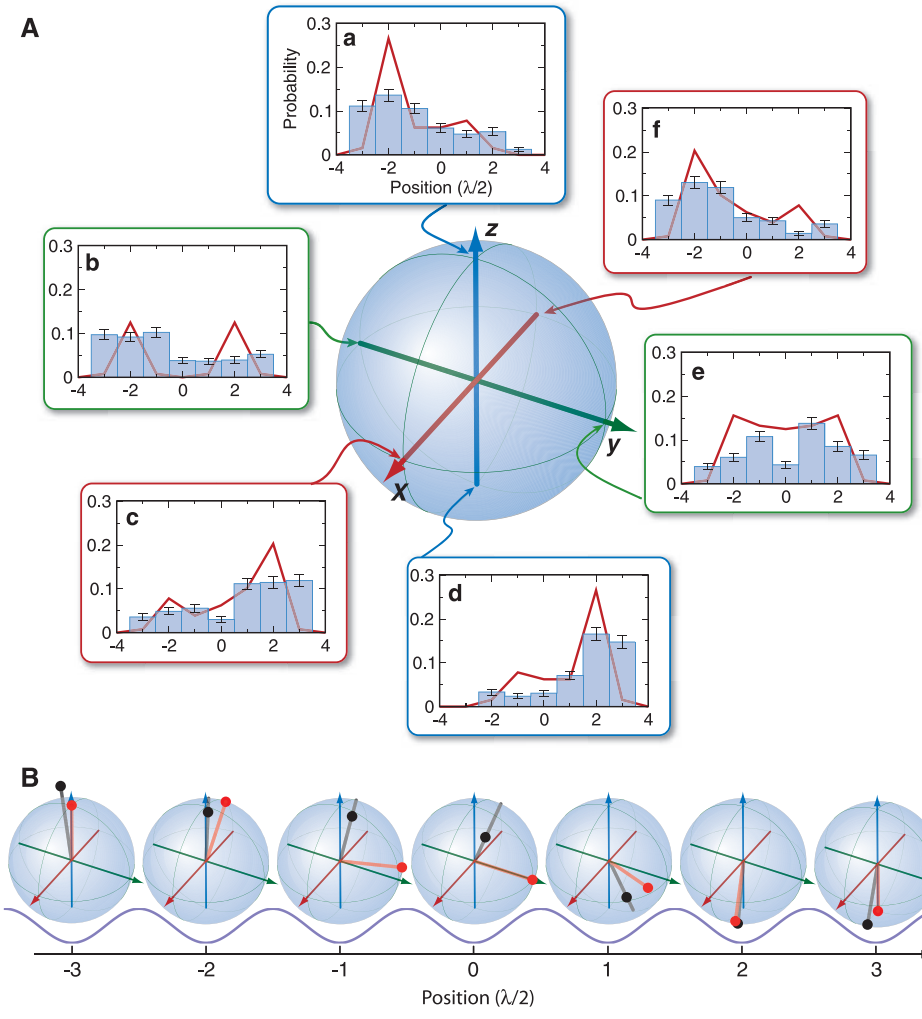

Fig. 3. (**A**) Local quantum state tomography of the atomic wave function after a six-step quantum walk. The distributions belong to the eigenstates of the Pauli spin operators $\hat{\sigma}_i (i = x, y, z)$: (a) $|0\rangle$ (+z axis), (b) $(|0\rangle - i|1\rangle)/\sqrt{2}$ (–y axis), (c) $(|0\rangle + |1\rangle)/\sqrt{2}$ (+x axis), (d) $|1\rangle$ (–z axis), (e) $(|0\rangle + i|1\rangle)/\sqrt{2}$ (+y axis), and (f) $(|0\rangle - |1\rangle)/\sqrt{2}$ (–x axis). (**B**) Reconstructed Bloch vectors at each position in the lattice. The tips of the reconstructed and ideally expected Bloch vectors are shown as black and red dots, respectively. The lines for Bloch vectors extend to the surface of the Bloch sphere to guide the eye; deviations from the surface illustrate the effect of decoherence and measurement errors.

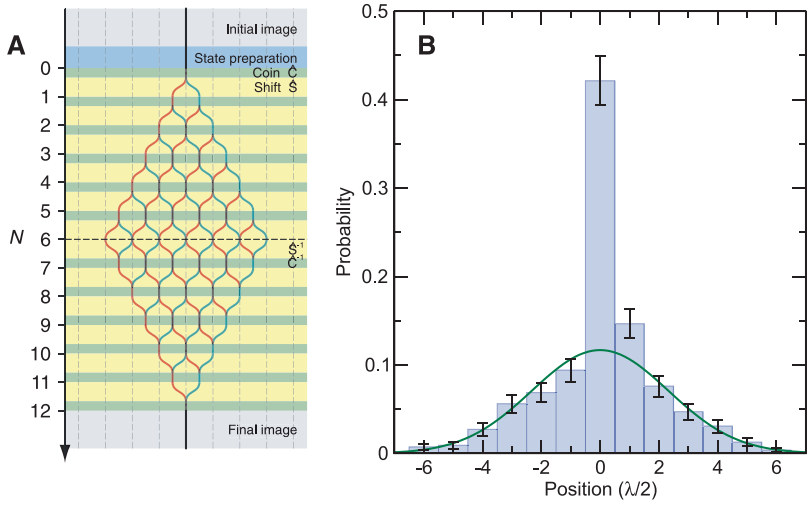

Fig. 4. (**A**) Time-reversal sequence for refocusing the delocalized state of a six-step quantum walk. After six steps, the total application of the coin and shift operator is reversed, where $(\hat{S}\hat{C})^{-1} = \hat{C}^{-1}\hat{S}^{-1}$. (**B**) The resulting probability distribution shows a pronounced peak at the center, to where, ideally, the amplitude should be fully refocused. We observe a refocused amplitude of 30%, surrounded by a Gaussian background (fitted curve).

walk is fully deterministic and unitary, the multipath interference can be reversed by inverting coin and shift operations.

We realize a quantum walk with single laser-cooled cesium (Cs) atoms, trapped in the potential wells of a 1D optical lattice (*12*) with site separation of $\lambda/2 = 433$ nm (here, λ is the wavelength of the lattice laser light). The atoms are thermal with a mean energy of $k_B \times 10$ μK, whereas the optical potential depth is $k_B \times 80$ μK (here, k_B is the Boltzmann constant). They are distributed among the axial vibrational states with a mean occupation number of $\bar{n}_{ax} = 1.2$. Initially, the atoms are prepared in the $|0\rangle \equiv |F = 4, m_F = 4\rangle$ hyperfine state by optical pumping, where F is the total angular momentum, and m_F its projection onto the quantization axis along the dipole trap axis. Resonant microwave radiation around 9.2 GHz coherently couples this state to the $|1\rangle \equiv |F = 3, m_F = 3\rangle$ state. A $\pi/2$ pulse of 4 μs initializes the system in the superposition $(|0\rangle + i|1\rangle)/\sqrt{2}$. Coin operators are realized in the form of Hadamard-type gates $\hat{C}:\{|0\rangle \rightarrow (|0\rangle - |1\rangle)/\sqrt{2}, |1\rangle \rightarrow (|0\rangle + |1\rangle)/\sqrt{2}\}$. The state-dependent shift operation is performed by continuous control of the trap polarization, moving the spin state $|0\rangle$ adiabatically to the right (whereas state $|1\rangle$ moves to the left) along the lattice axis within 19 μs (*26*). After N steps of coin operation and state-dependent shift, the final atom distribution is probed by fluorescence imaging. From these images, the exact lattice site of the atom after the walk is extracted (*27*) and compared to the initial position of the atom. Spin echo operations are combined with each coin operation (*26*), leading to a coherence time of 0.8 ms.

The final probability distribution $P_N(\xi)$ to find an atom at position ξ after N steps (Fig. 1) is obtained from the distance each atom has walked by taking the ensemble average over several hundreds of identical realizations of the sequence. Ideally, one expects a double-peak distribution with large amplitude close to the edges of the distribution (*7*). The relative heights of the left and right peaks—and therefore the symmetry—depend on the choice of the initial state. Decoherence gradually suppresses the pronounced peaks (*12*, *28*). We compare the measured distributions for the symmetric and asymmetric quantum walks of $N = 6$ steps (Fig. 1, D and E) with the theoretical expectations for the ideal case and find good agreement.

In contrast, a random walk distribution can be recovered by introducing decoherence after each step of the walk. Omitting the spin-echo from the coin operation and additionally waiting 400 μs between coin and subsequent shift operation destroys the phase relation between subsequent steps of the walk. The resulting probability distribution is described by a binomial distribution (Fig. 1G), as expected for a purely classical random walk.

The scaling of the width of the quantum and the random walk distribution with the number of steps is one of the most prominent distinguishing features. We have investigated this scaling behavior for both walks for up to $N = 24$ steps (Fig. 2). For the quantum walk, the width follows closely the expected linear behavior for up to 10 steps. The subsequent deviation is due to decoherence (*26*), which asymptotically turns the quantum walk into a classical random walk. In contrast, for the random walk, the typical square-root scaling is recovered.

To get a more detailed characterization of the wave function prepared by a six-step quantum walk sequence, we extract information on the internal state populations and relative phase by local quantum state tomography. This is based on site-resolved, state-selective detection combined with single-particle operations (*26*, *29*), providing a population distribution for each eigenstate of the Pauli spin operators $\hat{\sigma}_i (i = x,y,z)$ (Fig. 3). Essentially, at each lattice site, the internal quantum state is represented by a vector on the Bloch sphere, which we reconstruct from the result of the tomography. These Bloch vectors fit well to the theoretical prediction at the edges of the distribution, but they show increasing deviations in a region close to the initial site of the walk. At these lattice sites, matter wave interference occurs at almost every step during the sequence, which makes these lattice sites more sensitive to decoherence compared with sites further apart.

The local tomography, however, does not yield information about the off-diagonal elements of the position space density matrix, which essentially contain information about the phase relation between the wave function at different lattice sites rather than at each site. To demonstrate the spatial coherence of the state over all populated lattice sites, we invert the coin operation C^{-1}: $\{|0\rangle \rightarrow (|0\rangle + |1\rangle)/\sqrt{2}, |1\rangle \rightarrow (|0\rangle - |1\rangle)/\sqrt{2}\}$, as well as the shift operation, and continue the walk for six additional steps (Fig. 4). Ideally, the inversion acts as an effective time-reversal and refocuses the multipath interference pattern of the wave function back to the initial lattice site. We find partial refocusing of 30% of the atomic population to the expected lattice site reflecting the fraction of atoms which have maintained coherence throughout the sequence.

We have studied the quantum walk of single neutral atoms in an optical lattice and characterized the quantum state of the delocalized atom. We have found good agreement with the ideal case of a quantum walk for up to 10 steps. Inversion of the walk causes the delocalized wave function to refocus to the initial lattice site. Although the atoms in our experiments are thermally distributed among several vibrational states, we obtain large coherence over a macroscopic distance. In the ideal case, motional state and internal states factorize so that the coherence created in one degree of freedom is not affected by the other. We have found that, as soon as internal and external degrees of freedom are coupled by diabatic transport leading to vibrational excitations, for instance, the matter wave interference is quickly suppressed.

It will be interesting to investigate the behavior of quantum walks for different conditions when coin operations depend on position or time. In particular, monitoring the decay of coherence under the influence of different noise sources will further elucidate the transition from the quantum to the classical regime. Performing the quantum walk with more than one atom and enabling coherent interactions between the atoms (*30*) will realize first operational quantum cellular automata that can be probed by full quantum state tomography, opening another experimental route toward quantum information science.

References and Notes

1. G. Möllenstedt, H. Düker, *Z. Phys. A Hadrons Nucl.* **145**, 377 (1956).
2. O. Carnal, J. Mlynek, *Phys. Rev. Lett.* **66**, 2689 (1991).
3. M. S. Chapman *et al.*, *Phys. Rev. Lett.* **75**, 3783 (1995).
4. M. Weitz, T. Heupel, T. W. Hänsch, *Phys. Rev. Lett.* **77**, 2356 (1996).
5. L. Hackermüller, K. Hornberger, B. Brezger, A. Zeilinger, M. Arndt, *Nature* **427**, 711 (2004).
6. M. A. Schlosshauer, *Decoherence and the Quantum-to-Classical Transition* (Springer, Berlin, ed. 1, 2007).
7. J. Kempe, *Contemp. Phys.* **44**, 307 (2003).
8. M. Barber, *Random and Restricted Walks: Theory and Applications* (Gordon and Breach, New York, ed. 1, 1970).
9. H. C. Berg, *Random Walks in Biology* (Princeton Univ. Press, Princeton, NJ, revised ed., 1993).
10. E. F. Fama, *Financ. Anal. J.* **21**, 55 (1965); reprinted in *Financ. Anal. J.* **51**, 75 (1995).
11. A. M. Childs, *Phys. Rev. Lett.* **102**, 180501 (2009).
12. W. Dür, R. Raussendorf, V. M. Kendon, H. Briegel, *Phys. Rev. A* **66**, 052319 (2002).
13. R. J. Sension, *Nature* **446**, 740 (2007).
14. B. C. Travaglione, G. J. Milburn, *Phys. Rev. A* **65**, 032310 (2002).
15. P. L. Knight, E. Roldán, J. E. Sipe, *Phys. Rev. A* **68**, 020301 (2003).
16. J. Du *et al.*, *Phys. Rev. A* **67**, 042316 (2003).
17. C. A. Ryan, M. Laforest, J. C. Boileau, R. Laflamme, *Phys. Rev. A* **72**, 062317 (2005).
18. D. Bouwmeester, I. Marzoli, G. P. Karman, W. Schleich, J. P. Woerdman, *Phys. Rev. A* **61**, 013410 (1999).
19. B. Do *et al.*, *J. Opt. Soc. Am. B* **22**, 499 (2005).
20. H. B. Perets *et al.*, *Phys. Rev. Lett.* **100**, 170506 (2008).
21. H. Schmitz *et al.*, preprint available at http://arxiv.org/abs/0904.4214 (2009).
22. R. P. Feynman, A. R. Hibbs, *Quantum Mechanics and Path Integrals* (McGraw-Hill, New York, 1965).
23. R. Raussendorf, *Phys. Rev. A* **72**, 022301 (2005).
24. D. J. Shepherd, T. Franz, R. F. Werner, *Phys. Rev. Lett.* **97**, 020502 (2006).
25. K. G. H. Vollbrecht, J. I. Cirac, *Phys. Rev. A* **73**, 012324 (2006).
26. See the supporting material on *Science* Online.
27. M. Karski *et al.*, *Phys. Rev. Lett.* **102**, 053001 (2009).
28. V. Kendon, B. Tregenna, *Phys. Rev. A* **67**, 042315 (2003).
29. W. Rosenfeld, S. Berner, J. Volz, M. Weber, H. Weinfurter, *Phys. Rev. Lett.* **98**, 050504 (2007).
30. O. Mandel *et al.*, *Nature* **425**, 937 (2003).

31. We thank D. Döring, F. Grenz, and A. Härter for help in the construction of the apparatus and A. Rauschenbeutel for valuable discussions. We acknowledge financial support from the Deutsche Forschungsgemeinschaft (research unit 635) and European Commission (Integrated Project on Scalable Quantum Computing with Light and Atoms). M.K. acknowledges support from the Studienstiftung des deutschen Volkes, and J.-M.C. received partial support from the Korea Research Foundation grant funded by the Korean Government (Ministry of Education and Human Resources Development).

Supporting Online Material

www.sciencemag.org/cgi/content/full/325/5937/174/DC1
SOM Text
References

2 April 2009; accepted 3 June 2009
10.1126/science.1174436